Study of the forming limit of 6063 aluminum alloy perforated sheet under in-plane and out-of-plane stretching conditions

Houssem Eddine Lakache, Abdelghani May
Centre des Réalisations Mécaniques, École Militaire Polytechnique, BP 17, 16214, Algiers, Algeria.
lakache.houssem@gmail.com, https://orcid.org/0000-0003-2454-4216
abdelghani1980@yahoo.fr, https://orcid.org/0000-0002-3308-8796

Mohand Ould Ouali
LEC2M, Université Mouloud Mammeri Tizi Ouzou, BP 17RP, 15000, Tizi Ouzou, Algeria.
m_ouldouali@yahoo.fr, http://orcid.org/0000-0001-7958-4974

Abdelghani Mokdad
Laboratoire Des Techniques Avancées de Fabrication Et Contrôle, École Militaire Polytechnique, BP 17, 16214, Algiers, Algeria.
abdelghani1980@gmail.com

Lahouari Benabou
LISV, Université de Versailles Saint-Quentin dans les Yvelines, France.
lahouari.benabou@uvsq.fr, http://orcid.org/0000-0003-2345-6792

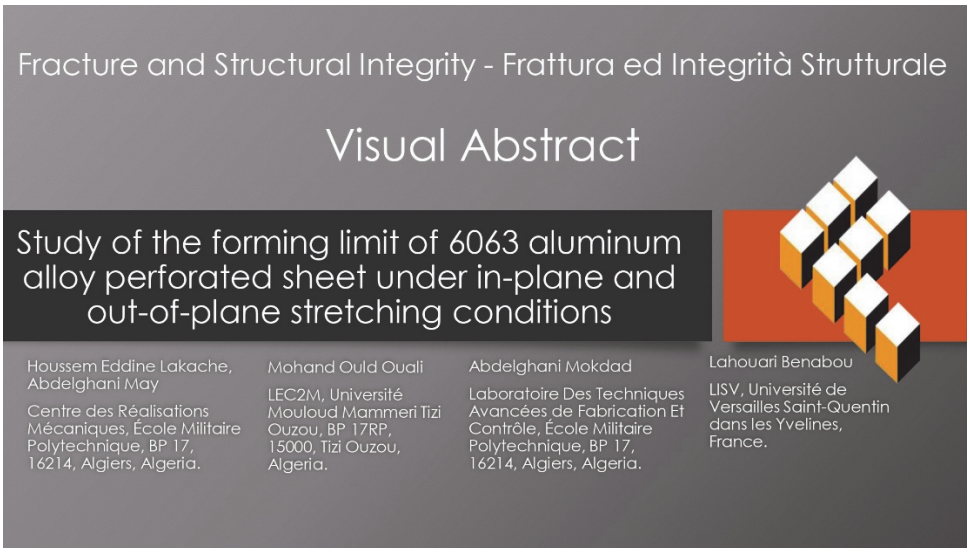

Citation: Lakache, H. E., May, A., Ould Ouali, M., Mokdad, A., Benabou, L., Study of the forming limit of 6063 aluminum alloy perforated sheet under in-plane and out-of-plane stretching conditions, Frattura ed Integrità Strutturale, 72 (2025) 62-79.

Received: 15.12.2024
Accepted: 24.01.2025
Published: 26.01.2025
Issue: 04.2025

KEYWORDS. Stamping, In-plane and out-of-plane stretching, FLD, AA6063, ABAQUS, Stereo-DIC.

INTRODUCTION

The use of aluminum alloys in industrial applications can be justified by its superior strength-to-weight ratio and remarkable formability. These attributes make aluminum alloys an appropriate material for examining their behavior under various loading circumstances [1]. The mechanical behavior of aluminum alloys has been extensively researched within the scientific community, with numerous studies aimed at comprehending their response to loads, environmental conditions, and their key mechanical properties, such as strength, stiffness, ductility, and toughness [2]. The outcomes of these studies have been instrumental in informing the development and design of various applications that rely on aluminum alloys.

In recent decades, metal stamping technology has emerged as a preferred alternative to other metal forming methods, including forging and die-casting, owing to its advantages in cost efficiency, production time, and improved quality characteristics [3]. Presently, approximately 20% of automotive components are produced using various stamping processes [4]. Stamping is categorized as a manufacturing process wherein the geometry, shape, and physical properties are modified. Defined by its fundamental principle, stamping is a process wherein thin-walled flat metal parts undergo shaping by punches and cutting dies to transform them into three-dimensional pieces. The stamping process can be further classified into various types, such as deep drawing and blanking, based on factors like temperature, deformation level, speed, and the final product shapes [5]. The addition of strategically placed perforation holes in stamped sheets serves to both reduce the overall weight of the sheet, which is crucial in applications where lightness is essential, such as in the automotive industry, and decrease costs by reducing the amount of material required, leading to manufacturing cost savings. Furthermore, these perforation holes can enhance the ductility of the material, facilitating the stamping process by reducing local stresses. Well-designed perforation holes can also assist in managing heat dissipation and contribute to aesthetic considerations.

In order to assess the deformability of thin sheet metals undergoing in-plane stretching, Keeler and Backofen [6] and Goodwin [7] introduced the widely recognized concept of the Forming Limit Diagrams (FLD). Initially reliant on experimental measurements, the determination of FLDs proved to be laborious, time-intensive, and associated with non-negligible costs, not to mention potential reproducibility challenges. To address these limitations, substantial efforts have been invested in recent decades towards devising theoretical indicators capable of predicting the limits of formability for thin sheet metals [8].

The MARCINIAK test method is used to construct the FLD, which involves using a cylindrical flat top punch with a central hole to stretch the test piece [9]. The NAKAZIMA test, commonly referred to as the Limiting Dome Height (LDH), is a widely recognized method that utilizes a hemispherical punch [10]. Several related studies based on the NAKAZIMA and MARCINIAK tests have been reported in the literature [11–12]. The improved Johnson-Cook constitutive model was employed by Wang et al. [13] to predict the FLDs of the Al–Mg–Li alloy sheet that are subsequently compared with the experimental FLDs obtained through NAKAZIMA tests. The study reveals that the improved Johnson-Cook effectively describes the stress-strain relationship. Other researchers have utilized the Johnson-Cook and modified Zerilli-Armstrong (m-ZA) models to assess the FLD of brass [14] and ASS 316L [15] sheets.

The stereo-Digital Image Correlation (stereo-DIC) technique enables the plotting of the FLDs and determination of the strain field [16]. In its multi-scale version, both minor and major strains can be measured between two successive images [17]. The technique involves a three-step process for each test. Firstly, a pair of images of the calibration cube is obtained, allowing the stereoscopic system to be calibrated for a specific measurement. Secondly, a pair of images of the stamping in its initial position is acquired. Finally, a pair of images of the stamping in its final position is obtained [18]. These steps are critical for ensuring accurate and reliable results.

The aim of this study is to determine the FLDs of the 6063 aluminum alloy for both Perforated Sheet Metal (PSM) and Non-Perforated Sheet Metal (NPSM) through a combined numerical and experimental approach. The experimental FLD are obtained by using the stereo-DIC technique during the stamping process for NAKAZIMA and MARCINIAK tests, with image analysis conducted using a specialized MATLAB data processing program. The predicted FLDs will be derived from the material's isotropic constitutive and failure process modeled using the Johnson-Cook model, employing finite element computations in the ABAQUS simulation environment.

EXPERIMENTAL STUDY

The investigation is centered on the use of an Al-Mg-Si aluminum alloy, with the designation AA6063 and chemical composition provided in Tab. 1. In the Fig. 1, we illustrate the metallographic microstructure of the AA6063 base metal following a polishing process and chemical etching with Keller reagent (3 ml HCl, 2 ml HF, and 20 ml H_2O)

during 15 seconds. The dark, dispersed spots within the α-Al light matrix correspond to secondary phase particles, typically Fe-rich intermetallic compounds such as AlFeSi or AlFeMnSi, as well as Mg_2Si particles that precipitate during the solidification and subsequent processing of the alloy. These particles are non-uniformly distributed in the microstructure, which can influence the mechanical properties and fracture behavior. The α-Al light matrix represents the primary aluminum solid solution, which contributes to the overall ductility of the material. As stated before, the aim of this work is to determine the FLDs of this material. So, the forming tests are carried out on a range of specimens of different widths obtained by cutting portions on two opposite-sides of a circular blank (see Fig. 2). This approach is adopted because it's well known that during sheet forming the resulting strain path essentially depends on the width of the blanks. The circular blank, with a thickness of 2 mm and a diameter of 170 mm, was served as the reference. The perforation holes have a 2 mm diameter. The eight distinct specimens are provided in Fig. 2, including perforated and non-perforated blanks.

Elements	Al	Mg	Si	Fe	Cu	Mn	Ti	Zn	Cr
wt.%	98.06	0.62	0.58	0.35	0.12	0.11	0.07	0.05	0.04

Table 1: Chemical composition (wt %) of the AA6063 alloy.

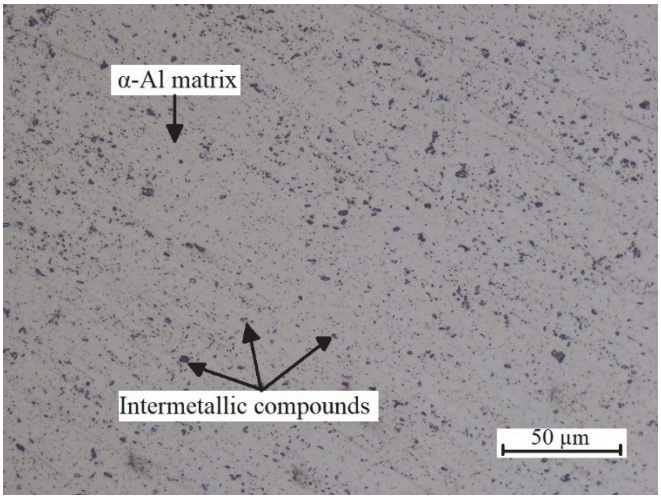

Figure 1: Metallography of AA6063 alloy.

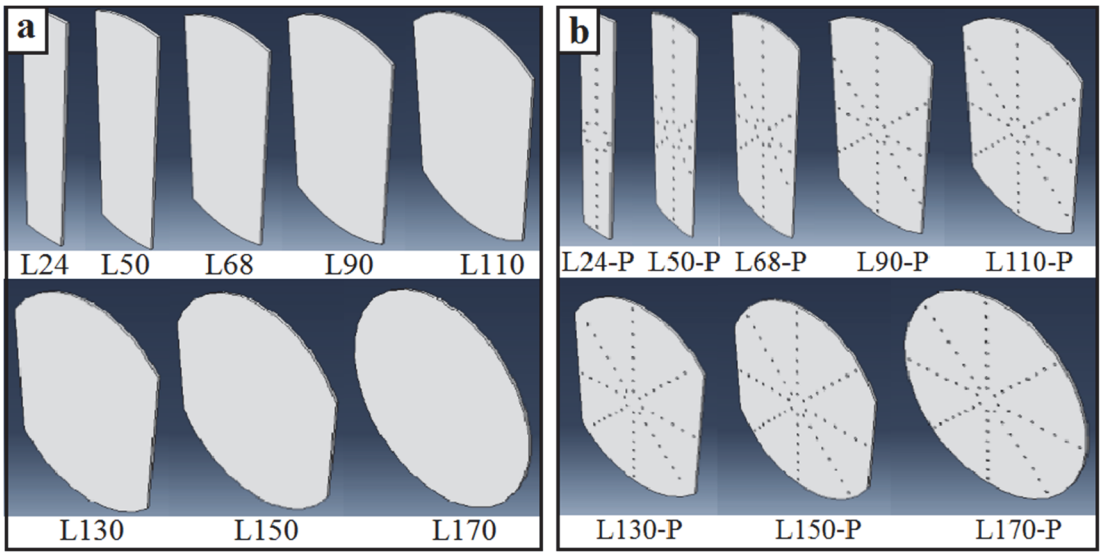

Figure 2: Geometry and dimensions of: a. NPSMs, b. PSMs.

The stamping experiments were conducted on a MAB hydraulic machine. The apparatus for making the stamping process has been designed to adapt to the stereo-DIC technique. This approach involves the use of two Charge Coupled Device

(CCD) cameras in conjunction with MATLAB software, as illustrated in Fig. 3a. The platform comprises of a support structure, threaded rods, upper and lower blank holders, and a punch. To capture an image during the stamping process, a mirror inclined at 45 degrees is placed underneath the stamping module (Fig. 3b).

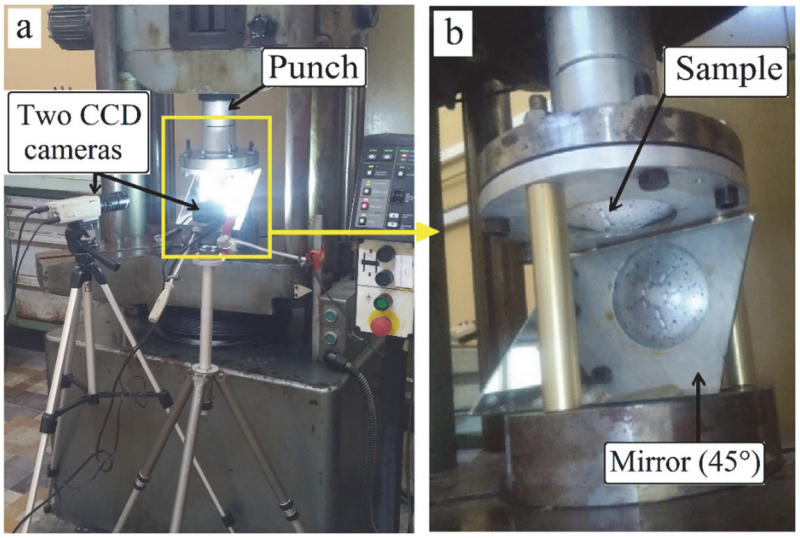

Figure 3: a. Stereo-DIC analysis platform, b. Stamping device.

The efficacy of the image correlation technique is contingent not only on the lighting conditions and camera resolution, but also on the preparation of the surface of the blanks being observed. To this end, a chemical treatment process, consisting primarily of removing the oxides and achieving surface cleanliness, was implemented. The pickling phase was executed through immersing the blanks in caustic acid with a concentration of 10 g/l for 3 min at 65°C. Subsequently, a bleaching treatment was carried out by dipping the blanks into a mixture of chromic acid (60 g/l) and sulfuric acid (180 g/l) for 30 s at 65°C, in order to restore their original whiteness. The blanks were then rinsed to ensure their surface purity, therefore demineralized water was utilized for the final rinse.

To accurately quantify the strain field of the specimen's surface during the stamping process by the stereo-DIC technique, a randomized pattern must be applied to the specimen under investigation. This is accomplished by applying black speckles to the surface through spray painting. This texture facilitates tracking of surface displacements when the sheet metal undergoes deformation. Furthermore, we gained a better understanding of the micromechanisms underlying the damage process by analyzing the fracture surfaces of the stamped specimens using a scanning electron microscope (SEM).

NUMERICAL MODELING

Johnson-Cook constitutive model

The development of plasticity is primarily attributed to the phenomenon of strain hardening resulting from deformation. Consequently, numerous studies have been conducted to develop models capable of describing this occurrence. In addition to strain hardening, material damage occurs due to the development of cracks that eventually lead to the complete failure of the specimen. To model the behavior of the aluminum alloy during shaping, the Johnson-Cook model [19] was chosen. Johnson and Cook proposed an empirical law based on experimental results and intended for rapid implementation in computer codes. This model proves effective in describing the stress-strain relations of metals subjected to large deformation and high strain rate [20].

$$\sigma\left(\varepsilon,\dot{\varepsilon},T^{*}\right)=\left[A+B\varepsilon^{n}\right]\left[1+C\ln\dot{\varepsilon}^{*}\right]\left[1-T^{*m}\right] \tag{1}$$

where σ is the equivalent flow stress, ε is the equivalent plastic strain, $\dot{\varepsilon}^{*}=\dot{\varepsilon}/\dot{\varepsilon}_{0}$ is the dimensionless plastic strain rate for $\dot{\varepsilon}_{0}=1\,s^{-1}$, and $T^{*}=\left(T-T_{0}\right)/\left(T_{m}-T_{0}\right)$ is the homologous temperature. T_{0} is the ambient temperature and T_{m} the melting temperature. The terms in the first set of brackets in Eqn. (1) give the stress as a function of strain for $\dot{\varepsilon}^{*}=1$ and

$T^{*m} = 0$, where A indicates the yield stress of the material (in MPa), B is the strain hardening constant (in MPa), and n being the strain hardening coefficient. The terms in the second set of brackets describe the effect of the strain rate, C being the sensitivity coefficient of strain rate strengthening. Ultimately, the components enclosed within the third set of brackets signify the impact of temperature or thermal softening. The coefficient, m, determines the stress's responsiveness to fluctuations in temperature. Tab. 2 presents the Johnson-Cook model parameters used in this study. These values were derived from experimental test results.

A (MPa)	B (MPa)	n	C (s^{-1})	m	Tm (K)
324	114	0.42	0.002	1.34	655

Table 2: Johnson-Cook constitutive model coefficients for AA6063.

Johnson-Cook failure model

The failure model presented herein has a basic form and uses a limited number of constants [21]. The material damage is characterized by a scalar variable D (Eqn. 2). Material failure occurs when D reaches the value of 1.

$$D = \sum \frac{\Delta \varepsilon}{\varepsilon_f} \tag{2}$$

where $\Delta\varepsilon$ is the equivalent plastic strain increment, which occurs during a cycle of integration, and ε_f is the equivalent plastic strain at fracture. The Johnson-Cook model presents the general expression for the equivalent plastic strain at fracture [19], as indicated in Eqn. 3:

$$\varepsilon_f = \left[d_1 + d_2 e^{d_3 \sigma^*} \right] \left[1 + d_4 \dot{\varepsilon}^* \right] \left[1 + d_5 T^* \right] \tag{3}$$

where d1, d2, d3, d4 and d5 are the damage constants of the model that are dependent on the material under investigation, and ε_f represents the strain at break, $\sigma^* = \sigma^m / \bar{\sigma}$ is the triaxiality strain rate, $\dot{\varepsilon}^*$ and T^* are the same parameters used in the constitutive model. In Eqn. (3), the criterion's three terms, enclosed in brackets, are clarified as follows: the first represents the triaxiality effect, the second describes sensitivity to the strain rate, and the last one accounts for thermal softening. Tab. 3 provides the values of the Johnson-Cook failure model constants used in the present study.

d1	d2	d3	d4	d5
-0.77	1.45	-0.47	-0.02	1.6

Table 3: Johnson-Cook failure model coefficients for AA6063.

RESULTS AND DISCUSSION

It is well known that DIC bypasses the main limitation of strain gauges and extensometers, which can only measure strain along a single axis. Indeed, under biaxial loading, such as bulge and FLC, and triaxial loading, conventional measurement with strain gauges and extensometers becomes imprecise. Additionally, the DIC technique overcomes another obstacle of measuring with strain gauges and extensometers which only allows measurements of deformation occurring directly underneath its attached surface. So these classic measurements can only capture local quantities. With these two advantages, DIC techniques have been adopted and successfully used in many studies, see for example [22–23]. In recent years, work has focused on Stereo-DIC, known as 3D-DIC, which allows the displacement field to be sampled both in-plane and out-of-plane of the specimen [24–25]. This new possibility is of great interest when measuring the material deformation during metal forming operations. In this study a Stereo-DIC technique with two CCD cameras is implemented and validated, then used to study the formability of a 6063 aluminum alloy during the stamping process as described below. The CCD cameras calibration process employs a target shaped like a plate, containing 25 squares (each side measuring 14 mm) of alternating colors white and black. Left and right photos of the calibration target are captured from two different

positions and angles as shown in Fig. 4, respectively. Following the completion of the calibration process for the two cameras, stereo calibration is subsequently carried out.

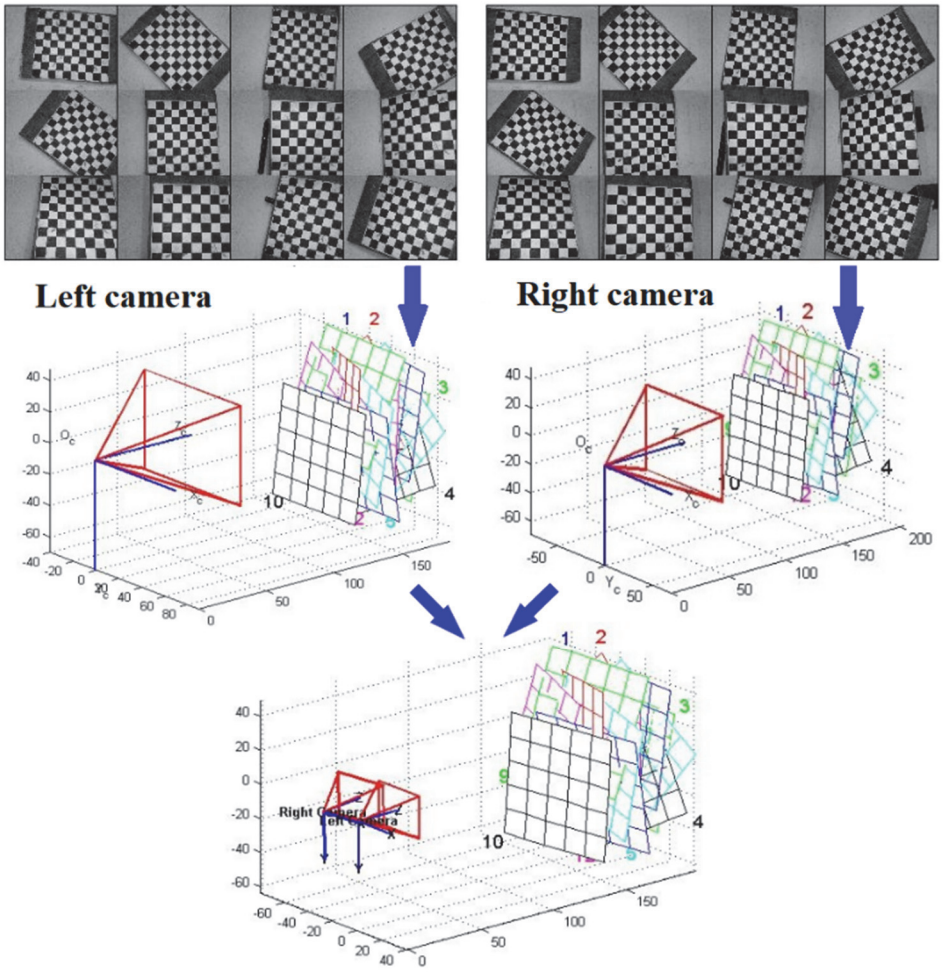

Figure 4: Principle of the stereo-calibration.

The validation of the calibration process was performed using a 3D calibration target, with two photographs captured using the left and right cameras. A 70 mm square was specifically chosen, and its dimensions were recalculated, with the resulting values detailed in Tab. 4. In Fig. 5, the distance measurements are graphically depicted against true distances, revealing an almost perfect correlation coefficient (≈1). This observation indicates that the measurement process's accuracy is highly satisfactory.

	Coordinates			Measured distance (mm)	Real distance (mm)	Error (%)
	X	Y	Z			
Side 1	-21.3160	-61.1616	25.3002	69.5357	70	0.7
Side 2	-65.2472	25.0045	7.1548	139.7754	140	0.4
Side 3	21.9152	61.2946	-26.1447	209.9242	210	0.3

Table 4: Validation results.

The experimental determination of FLDs requires the precise tracking of points within the speckle pattern on the blanks to determine their positions before and after the stamping process. Initially, photographs are captured from both left and right angles in the pre-stamped state. Similarly, photographs are taken in the post-stamped state. Fig. 6 serves as an illustration, depicting a non-perforated blank (L150) both before (Figs. 6a and 6b) and after (Figs 6c and 6d) deformation. The stamping

test concludes just before the onset of localized necking, and the points for stereo-correlation calculation are subsequently selected within this specific region.

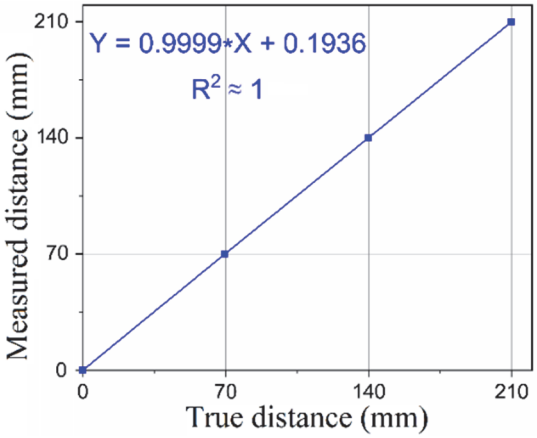

Figure 5: Validation curve of the calibration process.

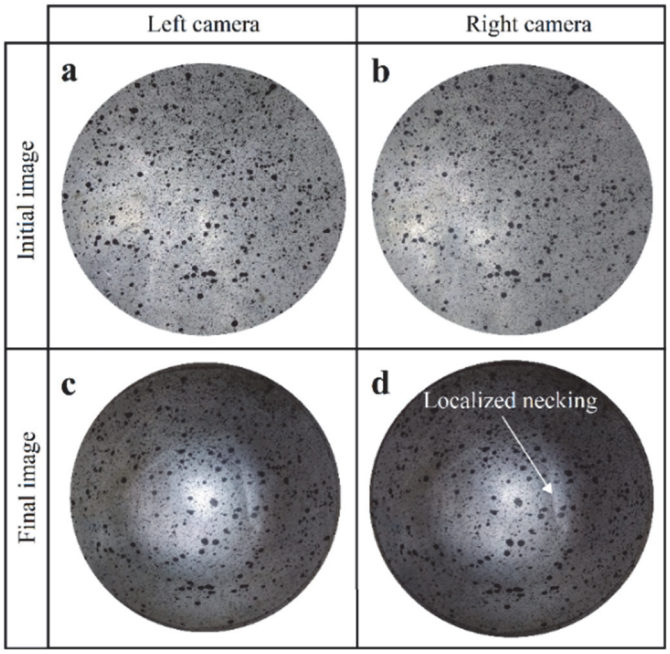

Figure 6: Image analysis by the stereo-DIC technique of the NAKAZIMA test for sample L170: initial image a. left and b. right, final image c. left and d. right.

NAKAZIMA test

The NAKAZIMA test results for NPSMs and PSMs are shown in Figs. 7a and 7b respectively. Their corresponding evolution of the applied load as a function of tool displacement are presented in Figs. 8a and 8b. As tool displacement increases, the applied load also increases, and although the curves exhibit a nearly identical appearance, there is a discernible difference in values. It is important to note that the applied load reaches significantly high levels for larger specimens, surpassing 35 kN for the largest NPSM.

Fig. 9 displays the FLDs resulting from the NAKAZIMA test for both types of blanks. Concerning NPSM specimens, it was observed that samples L170, L150, L130, and L110 experienced biaxial tension, indicated by positive strain along both the diameter and width. Conversely, the remaining NPSM samples, characterized by smaller widths, underwent uniaxial tension during the tests. As for PSM specimens, only samples L24, L50, and L68 were subjected to uniaxial tension, as the strain was positive exclusively along the Ox axis. In contrast, the remaining samples experienced biaxial tension throughout the stamping process.

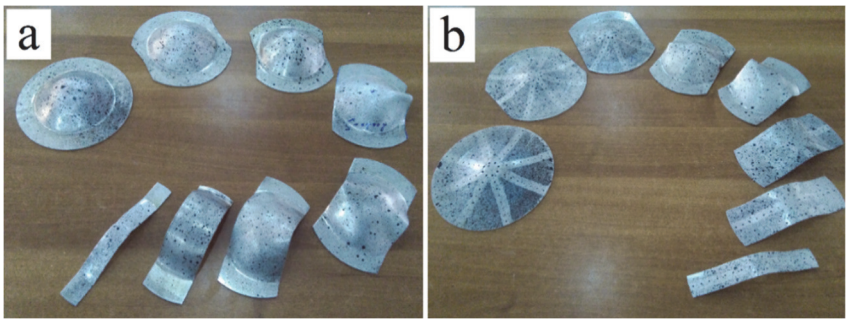

Figure 7: Stamped: a. NPSMs and b. PSMs.

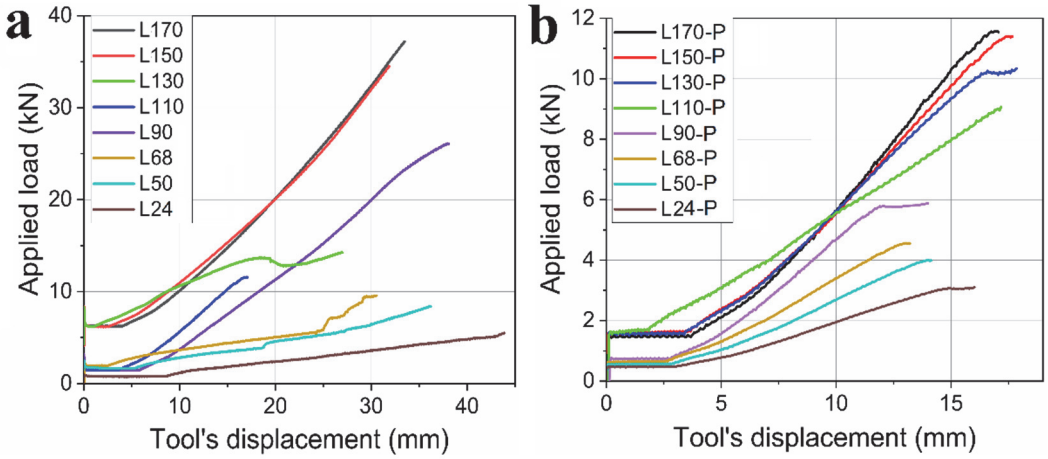

Figure 8: Applied loads for: a. NPSMs and b. PSMs.

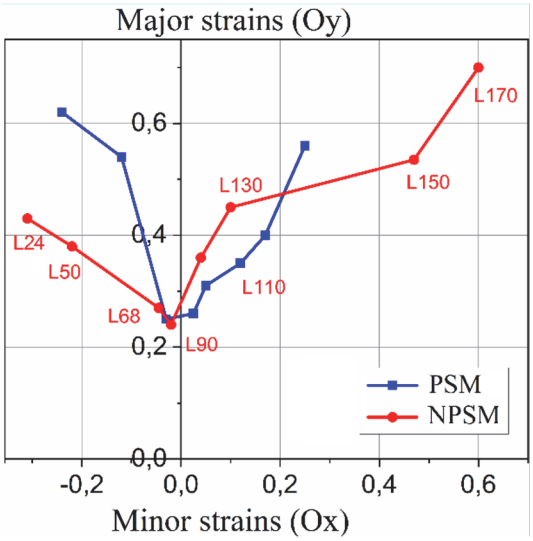

Figure 9: FLDs of NAKAZIMA test for the NPSM and PSM.

Fig. 10 presents a comparative analysis between experimentally observed fracture zones and numerically predicted ones. For illustrative purposes, the analysis concentrated on two specimens, specifically L150 and L170, in both PSM and NPSM variations. The findings suggest that the model accurately anticipates the locations of the fracture zones.

Tab. 5 presents both experimental and numerical results for the stamping force and maximum tool displacement corresponding to various widths for both types of blanks. The predicted stamping force values for all the considered samples are in good agreement with the experimental values, an increase in specimen width correlates with an elevation in stamping force. Stamping forces for PSMs fall within the range of 3 to 12 kN as shown in Fig. 11a, while NPSMs can require up to

39.3 kN of force (Fig. 11b). This significant variation can be attributed to the presence of perforation holes, which reduces the energy required for material deformation.

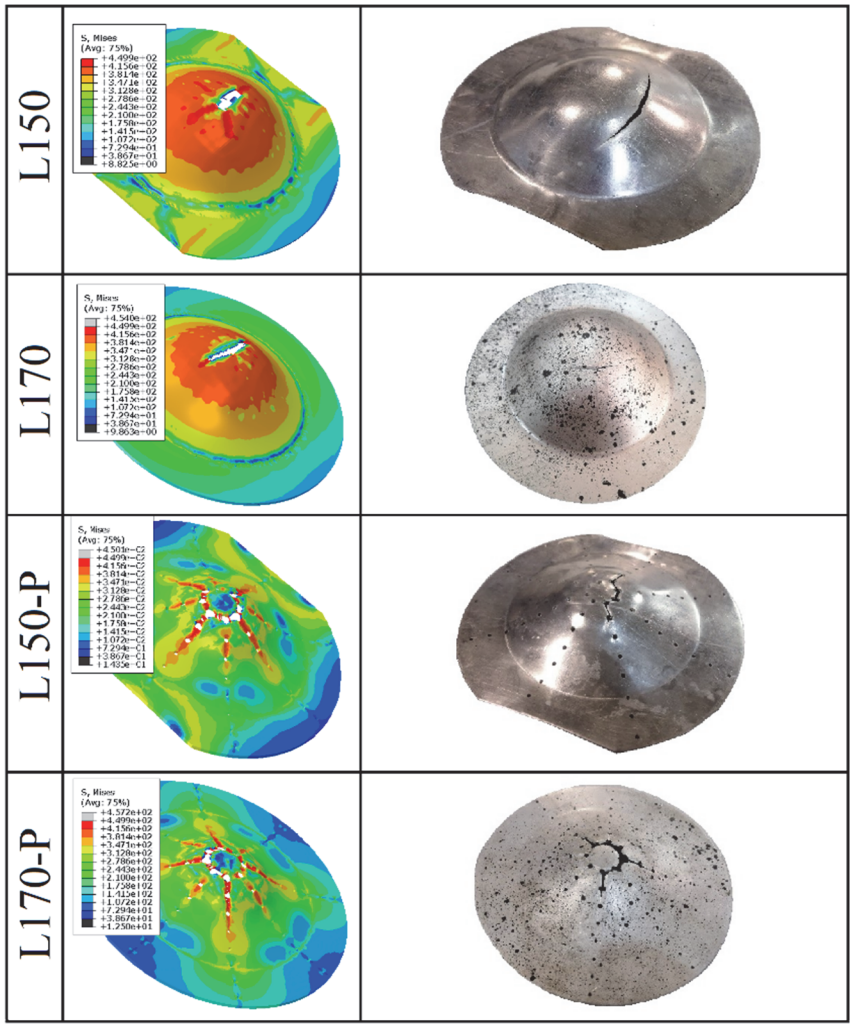

Figure 10: Comparison between experimental results and numerical predictions.

	Specimen width (mm)		24	50	68	90	110	130	150	170
NPSM	Stamping force (kN)	Num	5.0	7.8	9.1	12.5	15.2	26.8	34.6	37.8
		Exp	4.6	7.2	7.3	14.9	25.4	30.8	35.5	39.3
	Maximum tool displacement (mm)	Num	44.0	36.0	31.0	18.7	26.5	37.0	41.9	42.8
		Exp	41.6	36.3	25.2	22.0	26.4	34.4	44.3	44.5
PSM	Stamping force (kN)	Num	3.0	4.0	4.6	5.9	9.0	10.1	11.5	11.8
		Exp	5.0	5.5	7.5	8.5	10.7	10.8	10.5	11.3
	Maximum tool displacement (mm)	Num	17.8	14.9	13.6	14.0	16.4	17.5	17.3	17.2
		Exp	20.4	16.8	14.4	14.8	15.6	17.5	16.4	16.4

Table 5: Experimental and numerical values of stamping force and maximum tool displacement for NPSM and PSM specimens.

Although the tool displacement range differs between the two specimen types (See Figs. 12a and 12b), larger widths consistently result in relatively high maximum tool displacement values for both. However, for PSMs, the tool displacement remains consistently lower across the entire range of specimen widths.

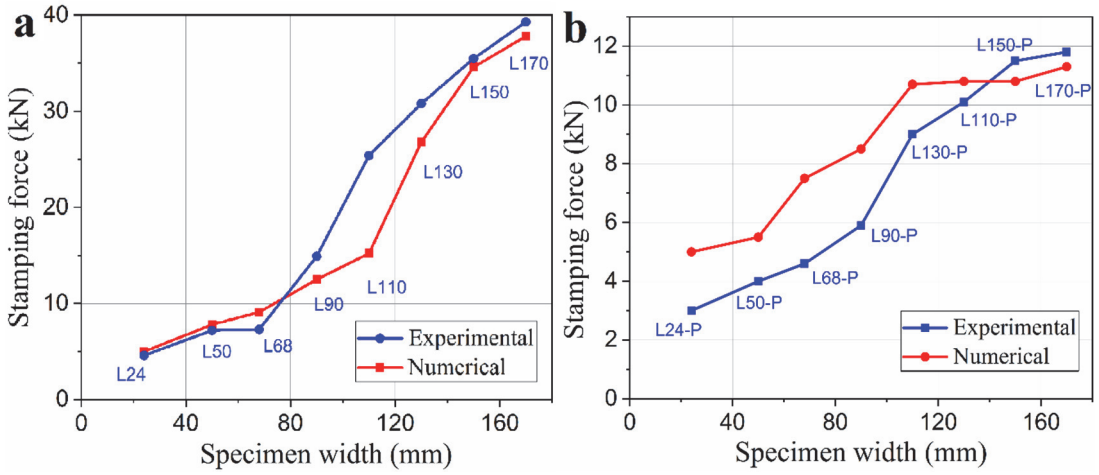

Figure 11: Numerical and experimental values of the stamping force for: a. NPSMs and b. PSMs.

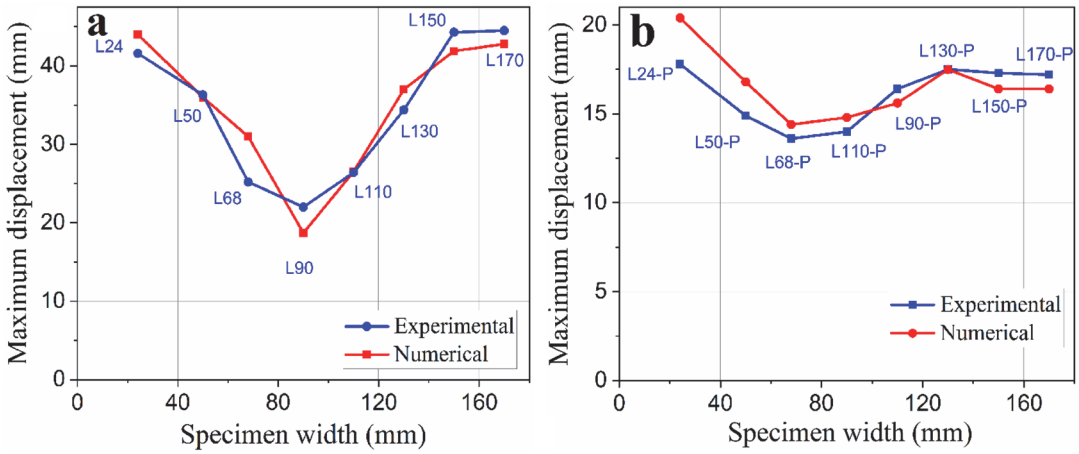

Figure 12: Numerical and experimental values of the maximum tool displacement for: a. NPSMs and b. PSMs.

Upon examining the test pieces, it was observed that there is a positive correlation between the width of the piece and the required stamping force. This result is anticipated, considering that a larger amount of material necessitates deformation, leading to increased resistance in the stamping process. In contrast, maximum tool displacement yielded high values for specimens with extensive widths, whereas for those with moderate widths, it decreased significantly.

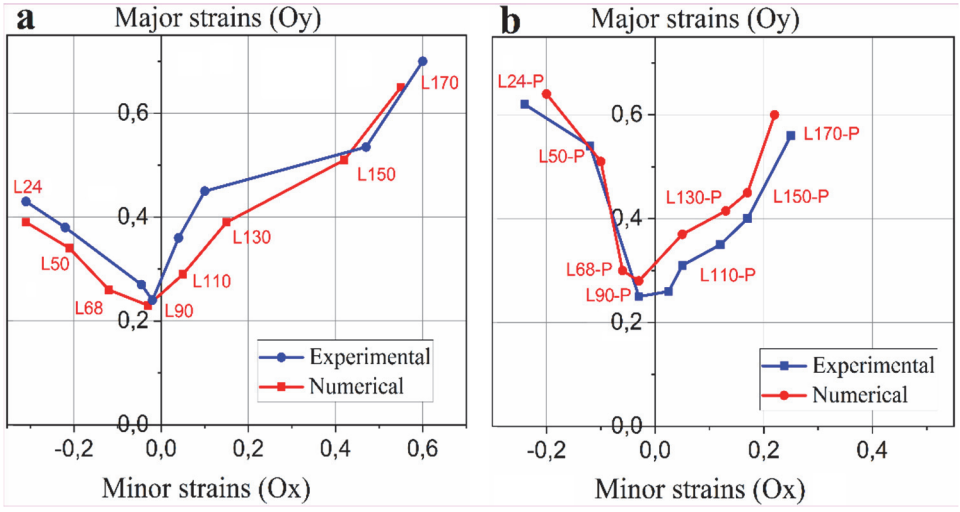

Figure 13: Numerical and experimental FLDs for: a. NPSMs, and b. PSMs.

The AA6063 FLDs from NAKAZIMA test, for both types of blanks are presented in Figs. 13a and 13b. The FLDs obtained from simulations and experiments show close alignment, but it is apparent that the simulated major and minor strain values exceed the experimental ones. The minor strains in the FLD of NPSMs are greater than those observed in the FLD of PSM ones. Nevertheless, the major strains exhibit similar values in both types of blanks.

Comparative study of the NAKAZIMA and MARCINIAK tests

Fig. 14 exhibits a comparative study of NAKAZIMA and MARCINIAK tests for NPSMs. It can be noticed that, in the MARCINIAK test, the concentration of the von Mises stress and rupture occurrence is primarily localized in the contact zone between the punch and the blank, where the lateral fracture occurred in the in-plane for all specimens. This is in contrast to the NAKAZIMA test, where rupture coincides with the central zone for blanks of medium and large widths (L68, L90, L110, L130, L150, and L170), while blanks with smaller widths (L24 and L50) experience rupture in the lateral zones away from the center.

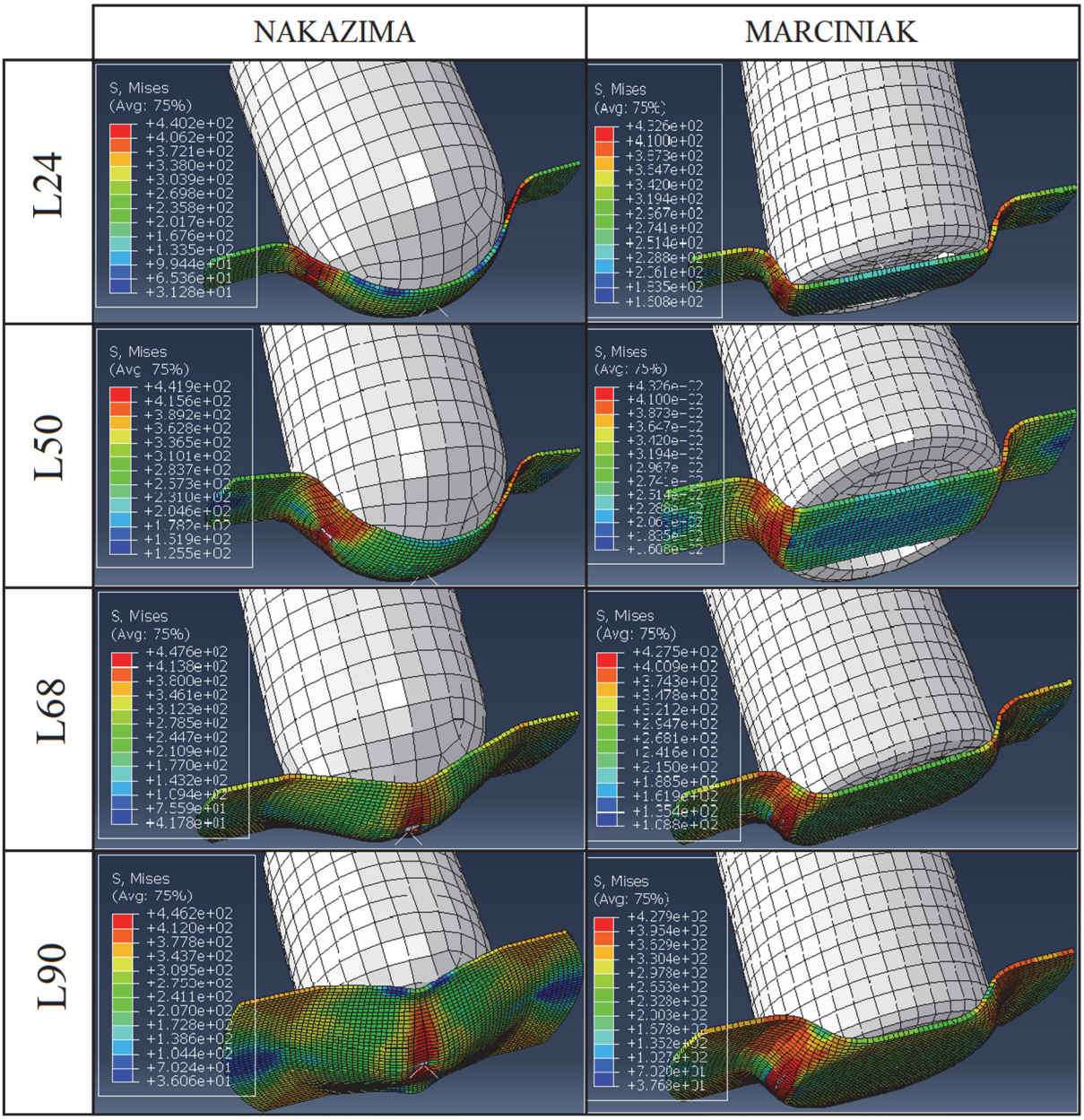

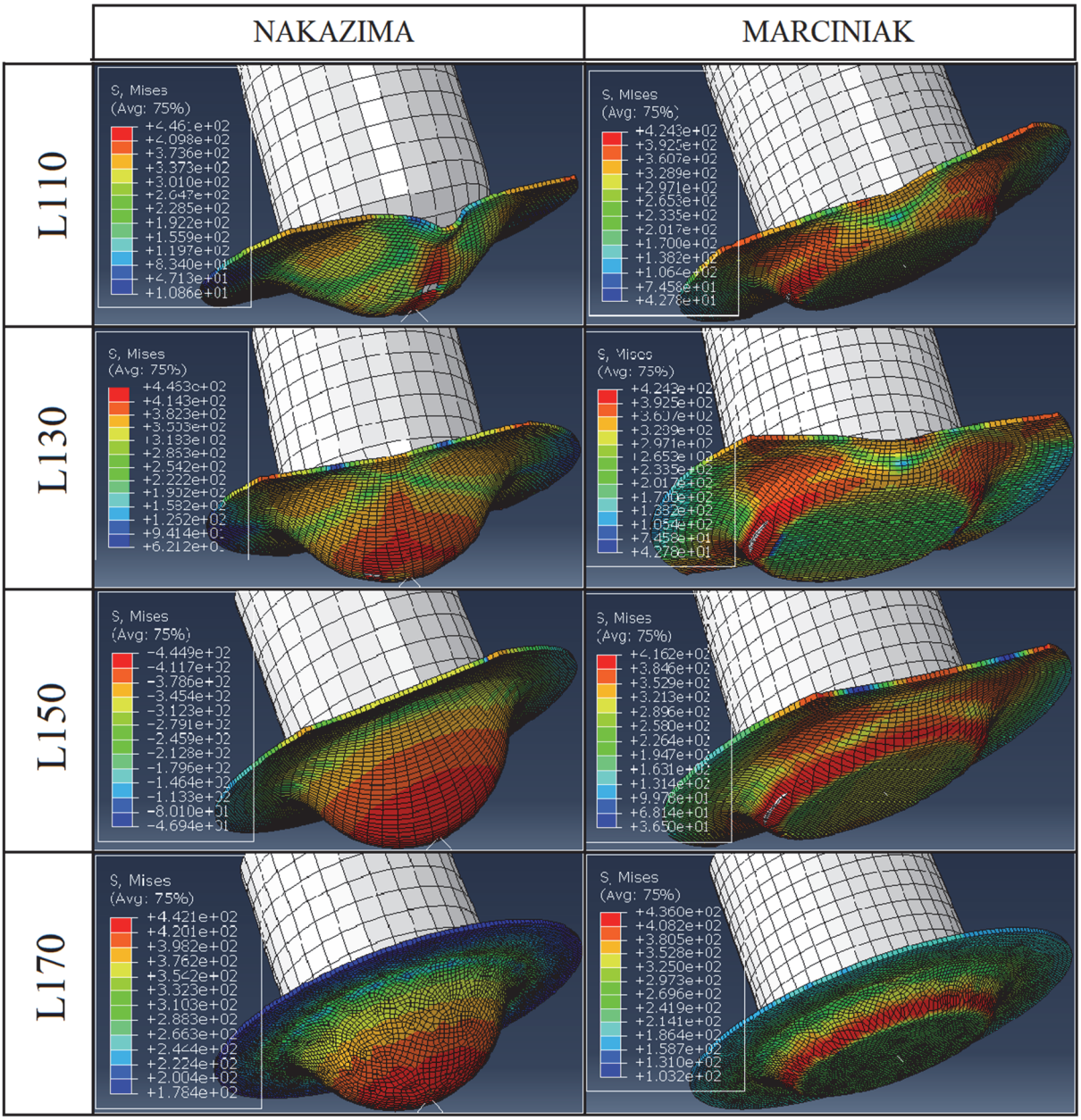

Figure 14: Von Mises stress distribution for NAKAZIMA and MARCINIAK tests.

Fig. 15a illustrates a comparison of the stamping force for the NAKAZIMA and MARCINIAK tests of NPSM specimens. It is obvious that the maximum forces in the two tests are of the same order of magnitude. In Fig. 15b, the maximum tool displacement is done for the two tests. In the MARCINIAK test, the maximum tool displacement remains consistently around 15 mm for all blanks. In contrast, the NAKAZIMA test shows a notable variation, ranging from 18.7 mm to 44.0 mm. This considerable fluctuation obtained although the stamping forces are close, illustrates that the NAKAZIMA test exhibits greater ductility, therefore lends itself well for the forming of NPSMs.

The FLDs in Fig. 16 are from MARCINIAK and NAKAZIMA. These tests reveal distinct forming domains. MARCINIAK FLD tends to exhibit lower major strain values for most blank widths compared to the NAKAZIMA FLD. This shows that the safe forming region obtained by NAKAZIMA test is higher than that obtained with MARCINIAK test. Furthermore, knowing that the deformation is mainly concentrated in the in-plane for the MARCINIAK test and out-of-plane during the NAKAZIMA test, it can be stated that the formability of the 6063 aluminum alloy sheet is higher out-of-plane.

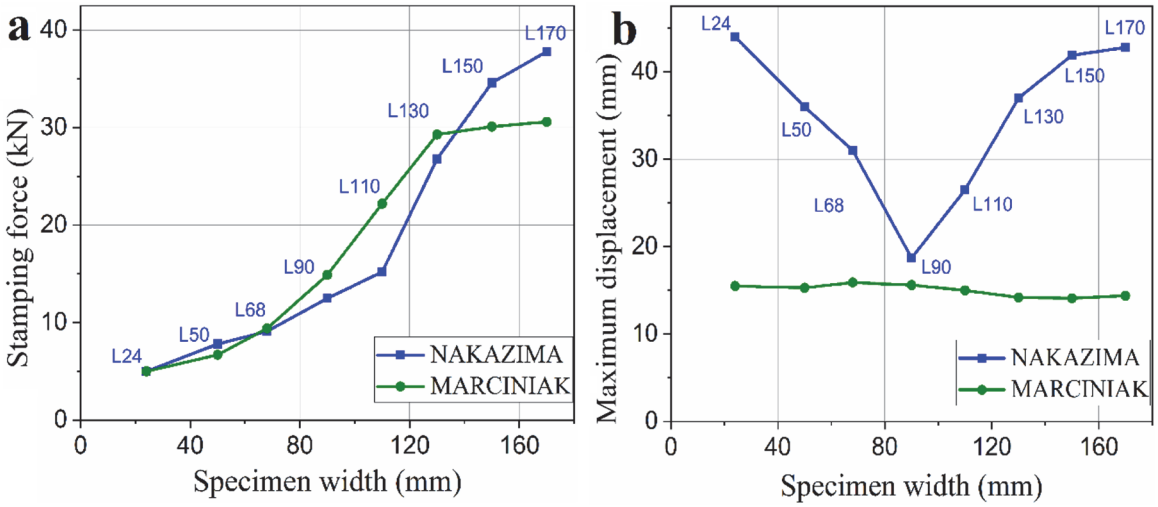

Figure 15: Comparison between the NAKAZIMA and MARCINIAK tests for NPSM: a. stamping force, and b. maximum tool's displacement.

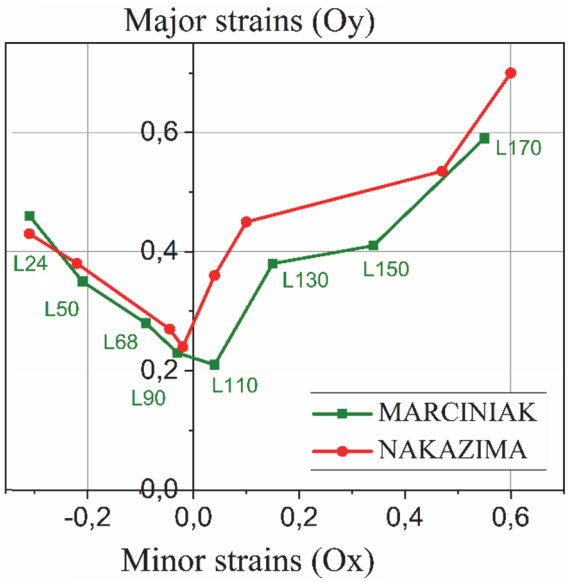

Figure 16: FLDs of NAKAZIMA and MARCINIAK tests.

Microstructural analysis of mechanical damage

Fig. 17 shows the mechanical behavior and microstructural evolution of the L150 NPSM specimen subjected to the NAKAZIMA test. The stamped specimen presented in Fig. 17a highlights the deformation induced by the test. Figs. 17b and 17c present SEM micrographs that reveal localized necking regions, indicative of severe plastic deformation concentrated in specific areas. This necking suggests the onset of instability in the material under the applied stress. Fig. 17d depicts material flow patterns, which provide insight into the redistribution of material during deformation. Finally, Fig. 17e offers a magnified view of the ductile deformation occurring prior to fracture, characterized by elongated voids and microstructural features associated with ductile failure. Together, these observations elucidate the progressive stages of deformation and failure mechanisms during the NAKAZIMA test of L150 NPSM, contributing to a deeper understanding of the material's response under complex loading conditions.

The post-failure crack morphology and associated fracture mechanisms are depicted in Fig. 18 for the L170 NPSM specimen subjected to the NAKAZIMA test. Fig. 18a displays the overall shape of the crack after failure, showcasing its irregular propagation path. Magnified views of the propagated crack, shown in Figs. 18b-18d, reveal features such as micro-void coalescence and secondary cracking, indicating progressive damage under tensile stress. Figs. 18e-18g illustrate the formation of new cracks, suggesting a complex interaction of stress fields and localized deformation zones. These new cracks likely originated from strain localization and material weakening in regions surrounding the primary crack. The figure highlights

the critical role of crack propagation and initiation mechanisms in determining the ultimate failure of the material, offering valuable insights into its fracture behavior under controlled deformation conditions.

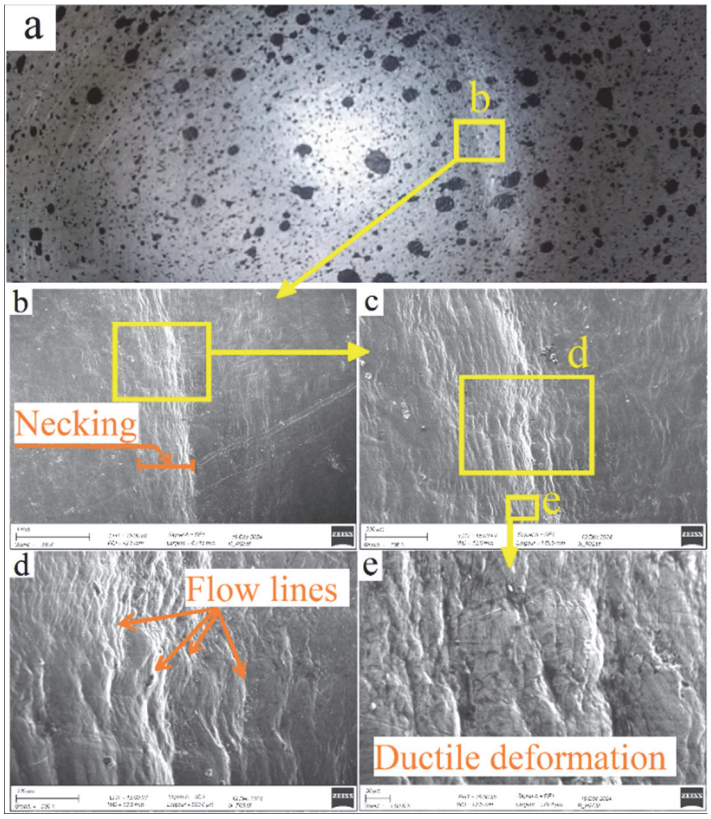

Figure 17: a. Stamped L150 NPSM specimen subjected to the NAKAZIMA test, b-c. SEM micrographs showing localized necking, d. Material flow, e. magnified view of ductile deformation prior to fracture.

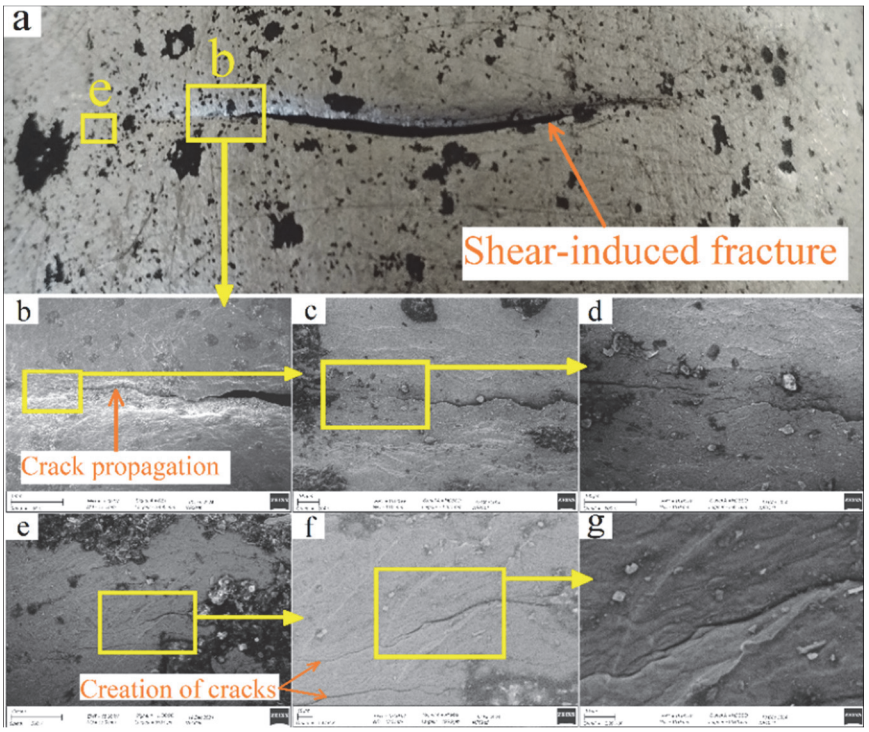

Figure 18: a. Post-failure crack morphology of L170 NPSM after the NAKAZIMA test, b-d. Magnified views of the propagated crack, e-g. Formation of new cracks.

Fig. 19 examines the fracture surface morphology of the L170 NPSM specimen following the NAKAZIMA test. Fig. 19a displays a SEM observation of the fracture surface, revealing distinct features indicative of ductile failure, such as dimples and micro-voids. The central region of the fracture surface, highlighted in Fig. 19b, emphasizes areas where significant plastic deformation occurred prior to failure. Fig. 19c offers a magnified view of the highlighted zone in Fig. 19b, showing finer details of the microstructural analysis. The combination of these observations provides valuable insights into the micro-mechanisms of ductile fracture, emphasizing the role of localized deformation, void nucleation, and growth in driving material failure.

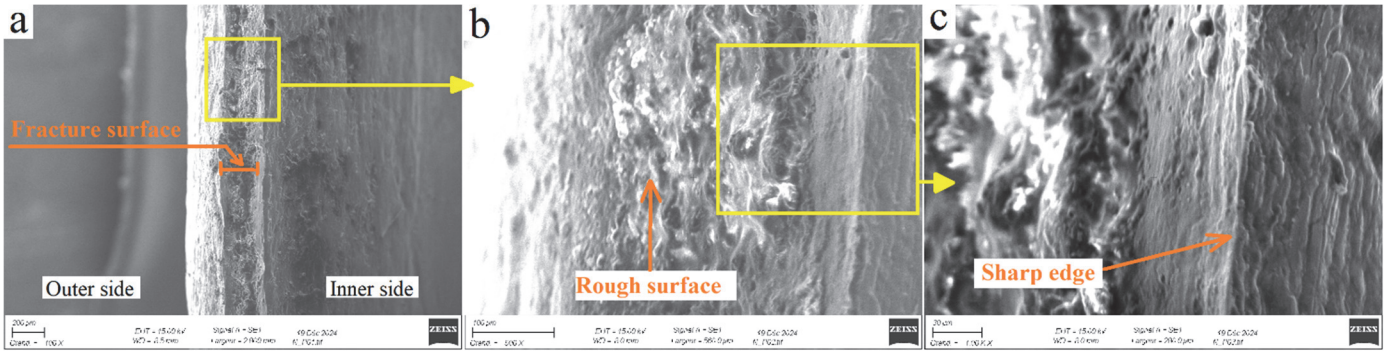

Figure 19: a. SEM observation of the fracture surface of L170 NPSM after the NAKAZIMA test, b. Central region of the fracture surface, c. Magnified view of the highlighted area in b.

Fig. 20 illustrates the progressive damage and fracture behavior of the L150-P PSM material subjected to the NAKAZIMA test, providing critical insights into void formation, crack propagation, and material failure. Fig. 20a presents a general view of the specimen post-test, highlighting the overall deformation and fracture patterns. The coalescence of voids is closely examined in Fig. 20b, emphasizing the progression of microvoids into cracks under stress. Fig. 20c displays the fracture surface, showcasing the material's failure characteristics, while Fig. 20d offers an enlarged view of the boxed region in Fig. 20c, revealing finer microstructural details, such as dimples, which indicate a ductile fracture mode. Finally, Fig. 20e demonstrates the ovalization of the hole shape, a clear indicator of the biaxial stretching experienced during the NAKAZIMA test.

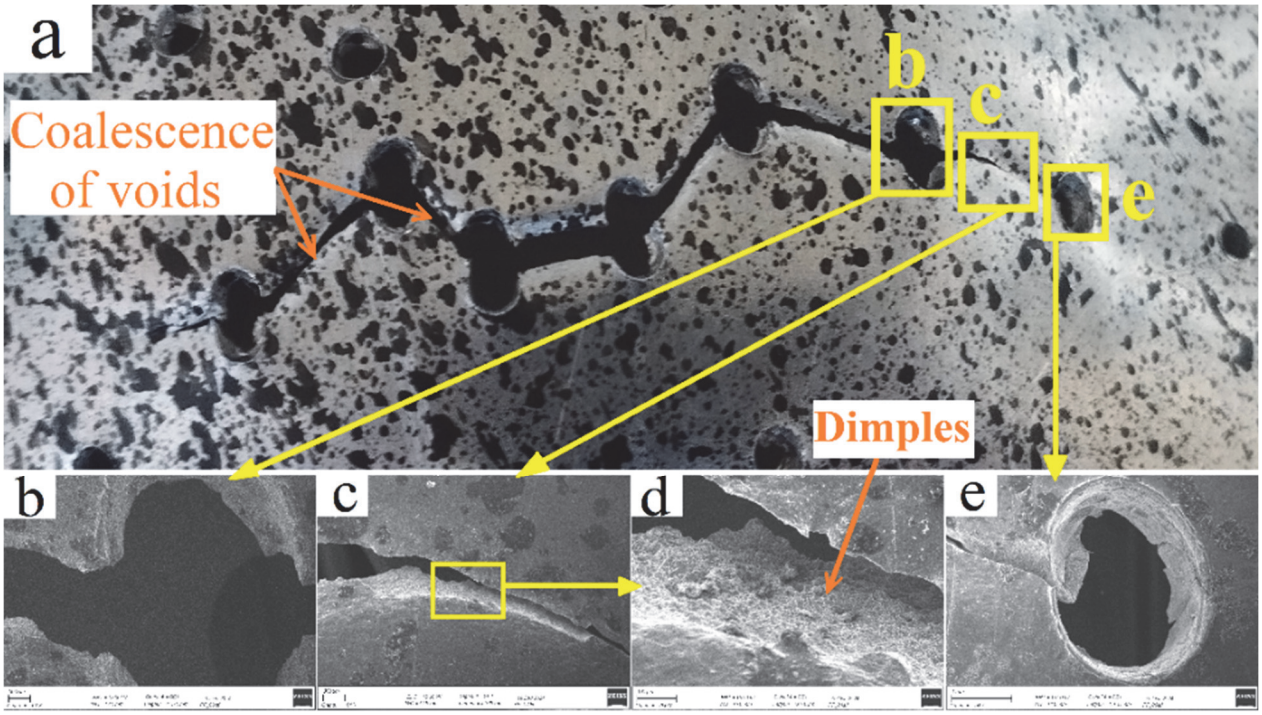

Figure 20: a. General view of L150-P PSM after the NAKAZIMA test, b. Coalescence of voids through crack propagation, c. Fracture surface, d. Enlarged view of the boxed area in c, e. Ovalization of the hole shape.

The detailed visual analysis of the fracture mechanisms in the L170-P PSM specimen following the NAKAZIMA test, as shown in Fig. 21, illustrates the progression from crack initiation to material failure. Fig. 21a offers a macro-image of the overall fracture morphology, highlighting the primary deformation and failure zones. The crack initiation zone is highlighted in Figs. 21b-21d, revealing early-stage material damage, such as localized stress concentrations and void nucleation. Fig. 21e captures the coalescence of voids, demonstrating how microscopic voids merge under tensile stress to form larger defects, initiating fracture propagation. Stages of crack propagation are depicted in Figs. 21f-21h, showing the development of fracture paths influenced by material anisotropy and stress distribution. Fig. 21i ultimately highlights the hole expansion, a result of significant plastic deformation and biaxial stretching.

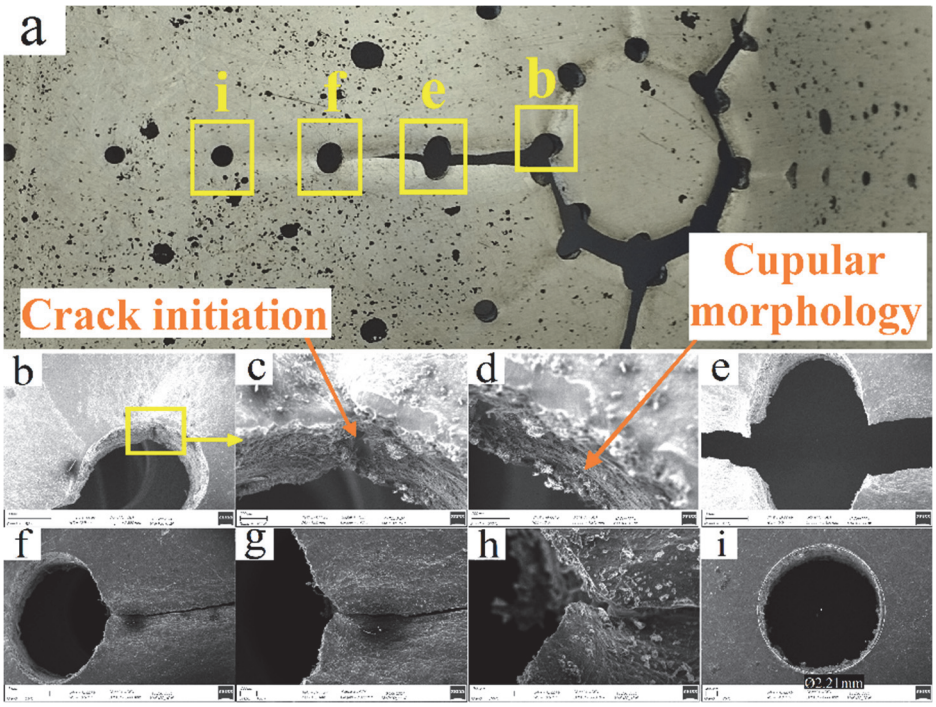

Figure 21: a. Macro-image of the fracture of the L170-P PSM specimen after the NAKAZIMA test, b-d. Crack initiation zone, e. Coalescence of voids, f-h. Crack propagation, i. Hole expansion.

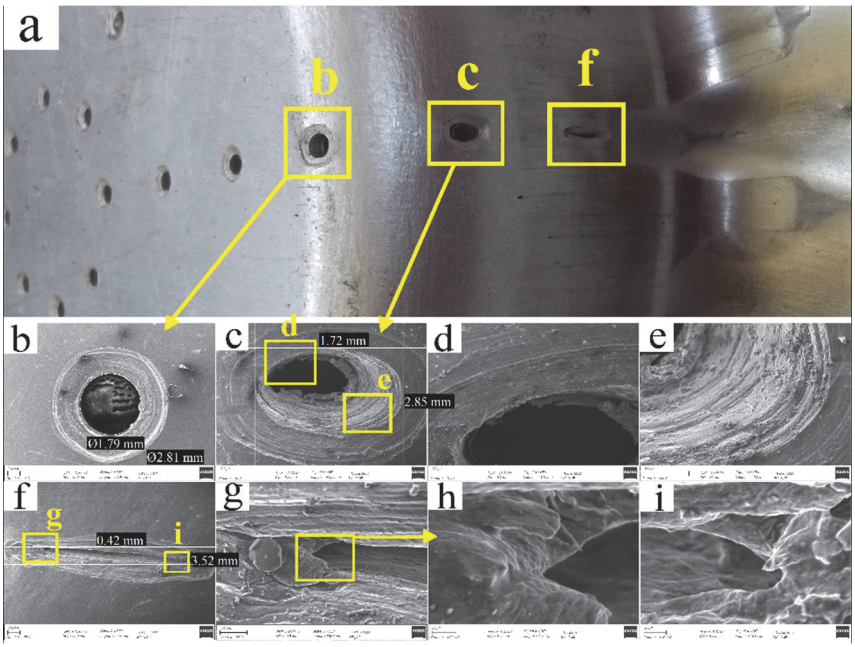

Figure 22: a. Various mechanisms of ductile deformation at different positions on L170-P PSM after the MARCINIAK test, b. Reshaping of the inner and outer hole contours, c-e. Hole deformation into an elliptical shape, f-i. Contraction of the hole.

The various ductile deformation mechanisms observed in the L170-P PSM material following the MARCINIAK test are illustrated in Fig. 22, emphasizing the complex interplay of stress and material response. In Fig. 22a, we identify distinct mechanisms of deformation at various positions on the specimen, showcasing the heterogeneity in ductile behavior across the material. Fig. 22b captures the reshaping of both the inner and outer hole contours, signifying the anisotropic nature of the deformation, while Figs. 22c-22e detail the transformation of the hole into an elliptical shape, demonstrating the material's response to biaxial stretching and localized thinning. Finally, Figs. 22f-22i highlight the contraction of the hole, providing insights into the material's capacity for strain localization and redistribution under applied loads.

CONCLUSION

A comprehensive numerical and experimental investigation of the stamping process was conducted to determine the FLDs of the 6063 aluminum alloy for both PSMs and NPSMs. The in-plane forming limit curves is obtained using the MARCINIAK test. The out-of-plane biaxial stretching is studied using the NAKAZIMA test. The key findings and conclusions can be summarized as follows:

- A Stereo-Digital Image Correlation, or 3D-DIC, is implemented and used for the measure the FLDs curves of the PSMs, and NPSMs.
- The numerical predictions using the constitutive and failure Johnson-Cook models are validated using the stereo-DIC technique and then used to explain the plastic behavior of the AA6063 material.
- The disparity in rupture locations and corresponding major and minor strains in the FLDs from MARCINIAK and NAKAZIMA tests highlights the particular stretching inherent in each test. In addition, a difference is observed in where and when the rupture occurs for each test.
- The safe forming region obtained by NAKAZIMA test is higher than that obtained with MARCINIAK test.
- The results of NAKAZIMA stamping operation confirm that the largest samples experienced biaxial tension, while uniaxial tension is predominant in smaller widths specimens.
- The maximum tool displacement in the NAKAZIMA testing based out-of-plane forming is double than that of the in-plane stretching MARCINIAK test for all the NPSM specimens.
- The microscopic analysis of the stamped specimens reveals various damage micromechanisms, including shear, crack initiation and propagation, and void coalescence, which depend on the test type, specimen geometry, and observed zone. The dominant fracture mode is identified as ductile.

REFERENCES

[1] Koubaa, S., Mars, J., Wali, M. and Dammak, F. (2017). Numerical study of anisotropic behavior of Aluminum alloy subjected to dynamic perforation, Int. J. Impact. Eng., 101, pp. 105–114. DOI: 10.1016/j.ijimpeng.2016.11.017.

[2] Guo, X., Zhu, S., Liu, X. and Liu, L. (2018). Experimental study on hysteretic behavior of aluminum alloy gusset joints. Thin-Walled. Struct., 131, pp. 883–901. DOI: 10.1016/j.tws.2018.02.033.

[3] Hashmi, M. S. J. (2014). Comprehensive materials processing, Newnes.

[4] Niemietz, P., Pennekamp, J., Kunze, I., Trauth, D., Wehrle, K. and Bergs, T. (2020). Stamping process modelling in an internet of production, Proc. Manuf., 49, pp. 61–68. DOI: 10.1016/j.promfg.2020.06.012.

[5] Klocke, F. and Kuchle, A. (2009). Manufacturing processes, Berlin, Springer.

[6] Keeler, S. and Backofen, W.A. (1963). Plastic instability and fracture in sheets stretched over rigid punches, ASM. Trans. Quart., 56, pp. 25–48.

[7] Goodwin, G. M. (1968). Application of strain analysis to sheet metal forming problems in the press shop, Sae. Trans., pp. 380–387.

[8] Y Bouktir, Y., Chalal, H. and Abed-Meraim, F. (2018). Prediction of necking in thin sheet metals using an elastic–plastic model coupled with ductile damage and bifurcation criteria, Int. J. Damage. Mech., 27(6), pp. 801–839. DOI: 10.1177/1056789517704030.

[9] Marciniak, Z. and Kuczyński, K. (1967). Limit strains in the processes of stretch-forming sheet metal, Int. J. Mech. Sci., 9(9), pp. 609–620. DOI: 10.1016/0020-7403(67)90066-5.

[10] K. Nakazima, T. Kikuma, K. Hasuka, (1968). Study on the formability of steel sheets. Yawata. Tech. Rep. 264, pp. 8517-8530.

[11] Cheong, K., Butcher, C. and Dykeman, J. (2018). The influence of the through-thickness strain gradients on the fracture characterization of advanced high-strength steels, SAE Int. J. Mater. Manuf., 11(4), pp. 541–552. DOI: 10.4271/2018-01-0627.

[12] Noder, J. and Butcher, C. (2019). A comparative investigation into the influence of the constitutive model on the prediction of in-plane formability for Nakazima and Marciniak tests, Int. J. Mech. Sci., 163, 105138. DOI: 10.1016/j.ijmecsci.2019.105138.

[13] Wang, Y., Zhang, C., Yang, Y., Wang, Y., Zhao, G. and Chen, L. (2020). The identification of improved Johnson-Cook constitutive model in a wide range of temperature and its application in predicting FLCs of Al–Mg–Li sheet, J. Mater. Res. Tech., 9(3), pp. 3782–3795. DOI: 10.1016/j.jmrt.2020.02.005.

[14] Singh, V. D., Mahalle, G., Hussain, M. M., Kotkunde, N. and Singh, S. K. (2024). Deformation behaviour and formability analysis of thin brass sheet: experiments and modelling, Aust. J. Mech. Eng., 22(2), pp. 296–313. DOI: 10.1080/14484846.2022.2087640.

[15] Dharavath, B., Morchhale, A., Singh, S. K., Kotkunde, N. and Naik, M. T. (2020). Experimental determination and theoretical prediction of limiting strains for ASS 316L at hot forming conditions, J. Mater. Eng. Perform., 29, pp. 4766–4778. DOI: 10.1007/s11665-020-04968-7.

[16] Pan, B., Yu, L. and Zhang, Q. (2018). Review of single-camera stereo-digital image correlation techniques for full-field 3D shape and deformation measurement, Sci. China. Technol. Sci., 61, pp. 2–20. DOI: 10.1007/s11431-017-9090-x.

[17] Li, J., Carsley, J. E., Stoughton, T. B., Hector Jr, L. G. and Hu, S. J. (2013). Forming limit analysis for two-stage forming of 5182-O aluminum sheet with intermediate annealing, Int. J. Plast., 45, pp. 21–43. DOI: 10.1016/j.ijplas.2012.10.004.

[18] Sutton, M. A., Yan, J. H., Tiwari, V., Schreier, H. W. and Orteu, J. J. (2008). The effect of out-of-plane motion on 2D and 3D digital image correlation measurements, Opt. Laser. Eng., 46(10), pp. 746–757. DOI: 10.1016/j.optlaseng.2008.05.005.

[19] Johnson, G. R. and Cook, W. H. (1985). Fracture characteristics of three metals subjected to various strains, strain rates, temperatures and pressures, Eng. Fract. Mech., 21(1), pp. 31–48. DOI: 10.1016/0013-7944(85)90052-9.

[20] Bobbili, R., Paman, A. and Madhu, V. (2016). High strain rate tensile behavior of Al-4.8 Cu-1.2 Mg alloy, Mater. Sci. Eng. A., 651, pp. 753–762. DOI: 10.1016/j.msea.2015.11.030.

[21] Johnson, G. R. (1980). Materials Characterization for computations involving severe dynamic loading, In Proc. Army. Symp. Solid. Mech., pp. 62–67.

[22] Qi, J., Xu, M., Zhang, W., Liu, Y. and Dai, X. (2022). Defect detection of pipeline inner surface based on coaxial digital image correlation with hypercentric lens, Mater., 15(21), 7543. DOI: 10.3390/ma15217543.

[23] Seo, S., Ko, Y. and Chung, M. (2022). Evaluation of field applicability of high-Speed 3D digital image correlation for shock vibration measurement in underground mining, Remote. Sens., 14(13), 3133. DOI: 10.3390/rs14133133.

[24] de Deus Filho, J. C. A., da Silva Nunes, L. C. and Xavier, J. M. C. (2022). iCorrVision-2D: An integrated python-based open-source Digital Image Correlation software for in-plane measurements (Part 1), SoftwareX., 19, 101131. DOI: 10.1016/j.softx.2022.101131.

[25] Nunes, L. and Xavier, J. (2022). iCorrVision-3D: An integrated python-based open-source Digital Image Correlation Software for in-plane and out-of-plane measurements (Part 2), SoftwareX., 19, 101132. DOI: 10.1016/j.softx.2022.101132.